



Structure/redox/activity relationships in $\text{CeO}_2/\text{CuMn}_2\text{O}_4$ CO-PROX catalysts

A. Elmhamdi^a, L. Pascual^b, K. Nahdi^a, A. Martínez-Arias^{b,*}

^a Laboratoire d'Application de la Chimie aux Ressources et Substances Naturelles et à l'Environnement, Faculté des Sciences de Bizerte, Université de Carthage, 7021 Zarzouma, Bizerte, Tunisia

^b Instituto de Catálisis y Petroleoquímica, CSIC, Campus de Cantoblanco, C/Marie Curie 2, 28049 Madrid, Spain



ARTICLE INFO

Article history:

Received 23 March 2017

Received in revised form 19 May 2017

Accepted 24 May 2017

Available online 26 May 2017

Keywords:

Nanostructured $\text{CeO}_2/\text{CuMn}_2\text{O}_4$ catalysts

CO-PROX

CO oxidation

Hydrogen purification

ABSTRACT

CuMn_2O_4 prepared by a microemulsion method is employed as support of ceria with different loading level (between 5 and 80 wt.%) and the CO-PROX properties of corresponding catalysts are explored. The catalysts have been characterized by XRD, S_{BET} measurement, HREM and XEDS, XPS and TPR, which allows establishing a complete model of the structural and chemical characteristics of the catalysts. The characterization results have been correlated with the analysis of CO-PROX catalytic properties performed by means of activity measurements complemented by *operando*-DRIFTS. Important differences in structural, redox and catalytic properties are detected as a function of the amount of ceria present in the catalyst. These are shown to depend basically on the size of the supported ceria nanocrystals as well as the fact that the increase in the ceria loading gradually increases the interfacial character of surface exposed sites of the support with important implications for the CO-PROX properties of the catalyst.

© 2017 Elsevier B.V. All rights reserved.

1. Introduction

Most efficient production of H_2 for feeding low temperature fuel cells is usually accomplished by a multi-step process that includes catalytic reforming of hydrocarbons or oxygenated hydrocarbons followed by the water–gas shift reaction (WGS) [1,2]. However, the platinum anode typically used in such type of fuel cells requires a hydrogen feed that is mostly free from CO in order to avoid its deactivation [2,3]. The high concentration of CO in the reforming stream cannot be brought down to concentration lower than 0.5 mol% after the two-stage WGS process because of thermodynamical limitations [4]. Since the CO level is still much higher than tolerated by low temperature fuel cell anodes [3,4], it has to be selectively treated to bring its concentration to very low level (typically below 100 ppm) in the H_2 -rich stream. Among different possibilities in this sense, the catalytic preferential oxidation of CO (CO-PROX) is considered as most simple and efficient process to attain such goal [5–7].

The catalysts for CO-PROX reported in the scientific literature can be basically classified into three types: (i) noble metal catalysts (typically Pt, but also Pd, Rh or Ir), usually supported on Al_2O_3 , SiO_2 or zeolites [6–14]; (ii) gold catalysts (supported on different oxides

like MnO_x , FeO_x , TiO_2 , Al_2O_3 , NiO , MgO or SnO_2) [6,7,15–17]; (iii) several kinds of base metal oxide catalysts, such as the oxides of Cu, Mn, Co, Ni and Fe, either alone or in combination with other oxides [6,7,18,19–21]. Among the latter, catalysts combining copper and cerium oxides have demonstrated outstanding potential for the process while they appear able to compete with less economically interesting noble metal catalysts; in particular, they generally show higher selectivity at full CO conversion than catalysts based on platinum-group metals while they appear more resistant to the presence of CO_2 than catalysts based on gold [6,7,22]. The particular ability of copper-ceria catalysts for the CO-PROX process has been essentially attributed to the synergistic redox properties produced upon formation of copper oxide-ceria interfacial sites, which are considered to constitute the active sites for the CO oxidation reaction [23–28].

On the other hand, another transition metal based material which is known to be a good catalyst for the oxidation reaction of CO is the hopcalite which is constituted by a mixture of oxides mainly based on copper-manganese mixed oxide [29–37]. The high activity of the hopcalite based catalysts for the oxidation of CO at low temperature is known since around 1920 which, along with its relatively low cost, justifies its use in masks for removing CO from breathing air [29,30]. However, studies related to the application of hopcalite-based materials for the CO-PROX process appear relatively scarce [38,39]. Hasegawa et al. have synthesized copper-manganese oxides using the sol-gel method and found them to

* Corresponding author.

E-mail address: amartinez@icp.csic.es (A. Martínez-Arias).

be highly active and selective for PROX at temperatures below 100 °C [38]. In turn, Valdés-Solís et al. have synthesized nano-sized copper manganite (CuMn_2O_4) via the silica aqua gel confined co-precipitation method and found it to be active for preferential oxidation of CO, even enhancing the performance of a Cu/CeO_2 reference catalyst, although certain deactivation occurred during the course of the process for both systems which has been attributed to the reduction of the catalyst surface [39]. On the other hand, the formation of solid solution between copper and manganese (or even the ternary $\text{Cu}-\text{Mn}-\text{Ce}$ mixed oxide) has been proposed as beneficial to the CO-PROX activity of $\text{CuO}-\text{MnO}_x-\text{CeO}_2$ catalysts [40]. Formation of $\text{Ce}-\text{Cu}-\text{Mn}-\text{O}$ ternary solid solution has been also invoked to explain enhanced CO-PROX properties of CuMnCeO ternary composite catalysts or Mn-doped $\text{CuO}-\text{CeO}_2$ [41,42].

Within this context, the present study is focused on the analysis of the CO-PROX properties of a copper-manganese mixed oxide (in the form of CuMn_2O_4 spinel) onto which different amounts of ceria promoter have been deposited. The approach is similar to that employed to conform inverse copper-cerium oxide catalysts (i.e. those in which copper oxide is used as the support for the dispersed ceria entities), which has been demonstrated to be an optimum configuration for this type of catalyst [43]. For mentioned purpose, a multi technique analysis (XRD, S_{BET} , HREM, XPS, TPR) has been performed for catalyst characterization while the catalytic activity tests have been complemented by *operando*-DRIFTS spectroscopy under reaction conditions with the aim of establishing on the whole structure/activity relationships for this type of catalyst/process.

2. Experimental

2.1. Sample preparation

CuMn_2O_4 , which exhibited optimum CO-PROX characteristics among a series of Cu-Mn mixed oxides in a previous study [38], was prepared by the microemulsion method. Two reverse microemulsions were mixed for this purpose. The first was prepared by including $\text{Cu}(\text{NO}_3)_2 \cdot 3\text{H}_2\text{O}$ and $\text{Mn}(\text{NO}_3)_2 \cdot 3\text{H}_2\text{O}$ in its aqueous phase with the appropriate molar ratios. The second one included tetramethylammonium hydroxyde pentahydrate (TMAH) as precipitating base into its aqueous phase. The microemulsions were in any case prepared by using n-heptane as major organic phase, Triton X-100 (Aldrich) as surfactant and hexanol as co-surfactant in volumes similar to those employed in previous works and in which further details of the preparation can be found [44]. After centrifugation and decantation, the resulting solid was rinsed with methanol, and then dried at 120 °C for 24 h and finally calcined in air at 500 °C.

Five catalysts of cerium supported on CuMn_2O_4 were prepared by incipient wetness impregnation of the CuMn_2O_4 support using aqueous solutions of cerium (III) nitrate hexahydrate with final cerium loading of 5, 10, 20, 40 and 80 wt.%. Following impregnation, the samples were dried overnight at 120 °C and calcined under air at 500 °C for 2 h. These samples will be referred to as $x\text{Ce}/\text{CuMn}$ with $x = \text{Ce}$ wt.% loading. ICP-AES chemical analysis displayed compositions for the samples as expected from nominal amounts employed during their preparation.

2.2. Techniques

The specific surface area of the calcined catalysts was determined by the BET method. N_2 adsorption isotherms were recorded with a Micromeritics 2100 automatic apparatus at liquid nitrogen temperature. The catalysts were degassed at 140 °C for 12 h before measurement of corresponding isotherms.

The X-ray photoelectron spectra (XPS) of the catalysts were collected using a Specs GmbH spectrometer under UHV condi-

tions ($P \approx 10^{-10}$ mbar) and using Mg K α radiation and a Phoibos 1509MCD energy analyzer. Binding energy values were estimated by using as reference the C 1s peak of contaminant carbon at 285.0 eV; in samples containing cerium, correct correction was further checked by adjusting the characteristic u'' peak of Ce 3d to 917.0 eV [45].

High resolution transmission electron microscopy (HRTEM) data as well as scanning transmission electron microscopy-high angle annular dark field (STEM-HAADF) images and X-ray energy dispersive spectra (XEDS) were recorded on a JEOL TEM/STEM2100F field emission gun transmission electron microscope operating at 200 kV and equipped with an EDS spectrometer Oxford INCA X-sight system. XEDS analysis was performed in STEM mode. Specimens were prepared by depositing small portions of the samples to be investigated from ethanol dispersion onto a nickel grid supporting a perforated carbon film.

Temperature programmed reduction (TPR) was measured in a flow system using 5% H_2/He premixed gas with flow rate of 30 mL min^{-1} . About 250 mg of catalyst was placed into a glass tube and pretreated under 10% O_2/He at 500 °C for 1 h using 100 mL min^{-1} flow rate and 10 °C min^{-1} ramp. The sample was then cooled to room temperature, thoroughly purged with inert gas and after switching to the reducing gas mixture it was heated up to 500 °C using 10 °C min^{-1} ramp. A Micromeritics Autochem II 2920 apparatus fitted with a TCD detector was employed for this measurement.

The catalysts calcined *in situ* (under oxygen diluted in He at 500 °C) were tested in a glass tubular catalytic reactor for their activity under an atmospheric pressure flow (using mass flow controllers to prepare the reactant mixture) of 1% CO, 1.25% O_2 and 50% H_2 (He balance), at a rate of 1000 $\text{cm}^3 \text{min}^{-1} \text{g}^{-1}$ (roughly corresponding to 80,000 h^{-1} GHSV) and using a heating ramp of 5 °C min^{-1} . The feed and outlet gas streams were analysed by gas infrared (Bruker Equinox 55 FTIR spectrometer, coupled to a multiple reflection transmission cell—Infrared Analysis Inc. “long path gas minicell”) and mass spectrometry (Pfeiffer Omnistar). Mass spectrometry analysis of the reactant mixture revealed the presence of ca. 0.2% H_2O , which originates from an impurity in the original H_2 . The experiments were made in the presence of such amount of water, taking into account that water is present in any reactant mixture resulting from reforming processes [1,2,4]; note also that the deactivating effect of water is an important issue in CO-PROX catalysis [46], while in addition catalysts based on Cu-Mn mixed oxides typically suffer such deactivating effect too [36]. No products other than those resulting from CO or H_2 combustion (i.e. CO_2 and H_2O ; note that possible contributions of WGS or reverse WGS must be residual under the conditions employed and, if at all, would take place only at temperatures higher than ca. 200 °C over this type of catalysts [25]) were detected in the course of the runs, in agreement with previous results on catalysts of this type [25,43]. On this basis, values of percentage conversion and selectivity in the CO-PROX process are defined as:

$$X_{\text{CO}} = \frac{F_{\text{CO}}^{\text{in}} - F_{\text{CO}}^{\text{out}}}{F_{\text{CO}}^{\text{in}}} \times 100$$

$$S_{\text{CO}2} = \frac{X_{\text{CO}}}{2.5X_{\text{O}2}} \times 100$$

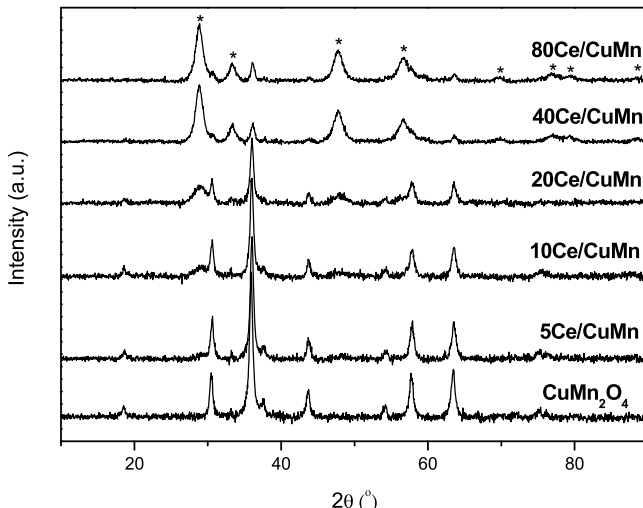
$$X_{\text{O}2} = \frac{F_{\text{O}2}^{\text{in}} - F_{\text{O}2}^{\text{out}}}{F_{\text{O}2}^{\text{in}}} \times 100$$

where X and S are percentage conversion and selectivity, respectively, and F is the (inlet or outlet) molar flow of the indicated gas. Note that during the competition between CO and H_2 oxidation

Table 1

Basic physico-chemical characteristics of the indicated catalysts.

Catalyst	S_{BET} (m^2g^{-1})	CeO ₂ crystal size ^a (nm)	CeO ₂ lattice parameter (Å)	Atomic ratio ^c		
				[Cu]/A ^d	[Mn]/A ^d	[Ce]/A ^d
CuMn ₂ O ₄	47			0.17	0.83	
5Ce/CuMn	41	n.d. ^b	n.d. ²	0.16	0.71	0.13
10Ce/CuMn	42	3.8	5.339			
20Ce/CuMn	56	4.4	5.375	0.12	0.46	0.42
40Ce/CuMn	55	7.0	5.401			
80Ce/CuMn	59	6.9	5.401	0.11	0.10	0.79

^a From XRD results upon application of the Scherrer equation to most intense (111) diffraction of this phase.^b Not sufficient resolution for reliable determination.^c From XPS results.^d A = ([Cu] + [Mn] + [Ce]).**Fig. 1.** X-ray diffractograms of the indicated catalysts. Peaks marked with an asterisk correspond to fluorite CeO₂.

the selectivity to CO₂ is related to the portion of consumed oxygen which produces CO₂.

Operando-DRIFTS experiments were carried out using a Bruker Equinox 55 FTIR spectrometer fitted with an MCT detector and a DRIFTS cell (Harrick). Aliquots of ca. 100 mg were calcined in situ (in a similar way as employed for the catalytic tests) and then cooled to room temperature under diluted oxygen before introducing the reaction mixture and heating under a 5 °C min⁻¹ ramp, recording typically one spectrum (accumulating 20 scans) every 20 °C. The reactant gas mixture (the same as that employed for the catalytic activity tests) was prepared using mass flow controllers with ca. 100 cm³ min⁻¹ passing through the catalyst bed at atmospheric pressure, corresponding to conditions similar to those employed for the activity tests performed with the tubular reactor.

3. Results and discussion

3.1. Characterization

Table 1 collects specific surface area values obtained for the catalysts. Some decrease of the S_{BET} with respect to that of the parent CuMn₂O₄ support is detected for samples with cerium loading \leq 10 wt.% while it appreciably increases for samples with higher loading. This suggests, as will be discussed below, that ceria acts as a support pore blocker at the lower loading while it could provide main textural properties to the samples at higher loading.

The X-ray diffractograms obtained for the various samples are displayed in **Fig. 1**. The CuMn₂O₄ support shows peaks corresponding to those expected for the spinel phase of this compound in

which the tetrahedral and octahedral sites are assumed to be occupied by Cu²⁺ and Mn³⁺ cations, respectively [47]. Average crystal size, using the Scherrer equation, for such phase is of 16.2 nm. As for the cerium-containing catalysts, a gradual growth of peaks due to the fluorite CeO₂ phase is detected with increasing the cerium loading. These appear as poorly resolved wide contributions for 5Ce/CuMn and 10Ce/CuMn samples while they become more apparent at higher cerium loading. Analysis of the width of most intense (111) peak of ceria at ca. 29° (in 2θ) evidences a growth of the average crystal size for this phase upon increasing the Ce loading up to 40 wt.% Ce after which it apparently stabilizes at ca. 7 nm, **Table 1**. In turn, analysis of the lattice parameter of the CeO₂ crystals reveals an apparent decrease with decreasing the Ce loading for samples with loading below 40 wt.%, **Table 1**. This must be related to the introduction of manganese or copper heterocations in the fluorite lattice, leading to lattice contraction [40,41,48]. It is known in this sense that the degree of lattice contraction can be determined by the oxidation state of the heterocationic dopant (in particular in the case of Mn) as well as by their solubility limit [25,49]. These could however be strongly influenced by the crystal size and a relatively small doping degree and lattice contraction is apparently attainable for relatively large particles [25,49,50]. The situation can be however reverted for very small crystals and a fluorite lattice parameter as small as 5.194 Å (in comparison with that of pure CeO₂ of ca. 5.410 Å) has been reported for a Ce-Mn mixed oxide of ca. 1.5 nm crystal size; this has been attributed to the formation of Mn_{0.5}Ce_{0.5}O_x solid solution with manganese present as Mn⁴⁺ species [51]. Samples 40Ce/CuMn and 80Ce/CuMn also exhibit a lattice parameter slightly lower than that of pure CeO₂, **Table 1**, thus suggesting also a certain heterocationic doping of the fluorite lattice in those cases.

The structural analysis is complemented with characterization performed by HRTEM and related techniques STEM-HAADF along with XEDS analysis. **Fig. 2** shows representative HRTEM images of the analyzed catalysts. The support CuMn₂O₄ consists of agglomerates of primary nanocrystallites with a particle size around 15 nm (**Fig. 2a**), in agreement with XRD estimation. The DDP (Digital Diffraction Pattern) obtained from one crystallite in the inset of **Fig. 2(a)** shows the [110] zone axis of the spinel type structure (Fd-3m) corresponding to the CuMn₂O₄ phase.

HRTEM images of the CeO₂/CuMn₂O₄ samples with 5, 20 and 80 wt.% of CeO₂ are displayed in **Figs. 2b-d**. The two phases CeO₂ and CuMn₂O₄ appear usually as randomly superposed in the bulk. They can be however identified at the borders on the basis of interplanar distances measured on the HRTEM images: i.e. $d = 3.09$ Å, attributed to the interplanar distance between (111) planes of the fluorite CeO₂ phase and $d = 4.75$ Å for the (111) planes of the spinel CuMn₂O₄ phase. In any case, the CeO₂ particles appear to be round-shaped and forming aggregates of small nanocrystals with different sizes.

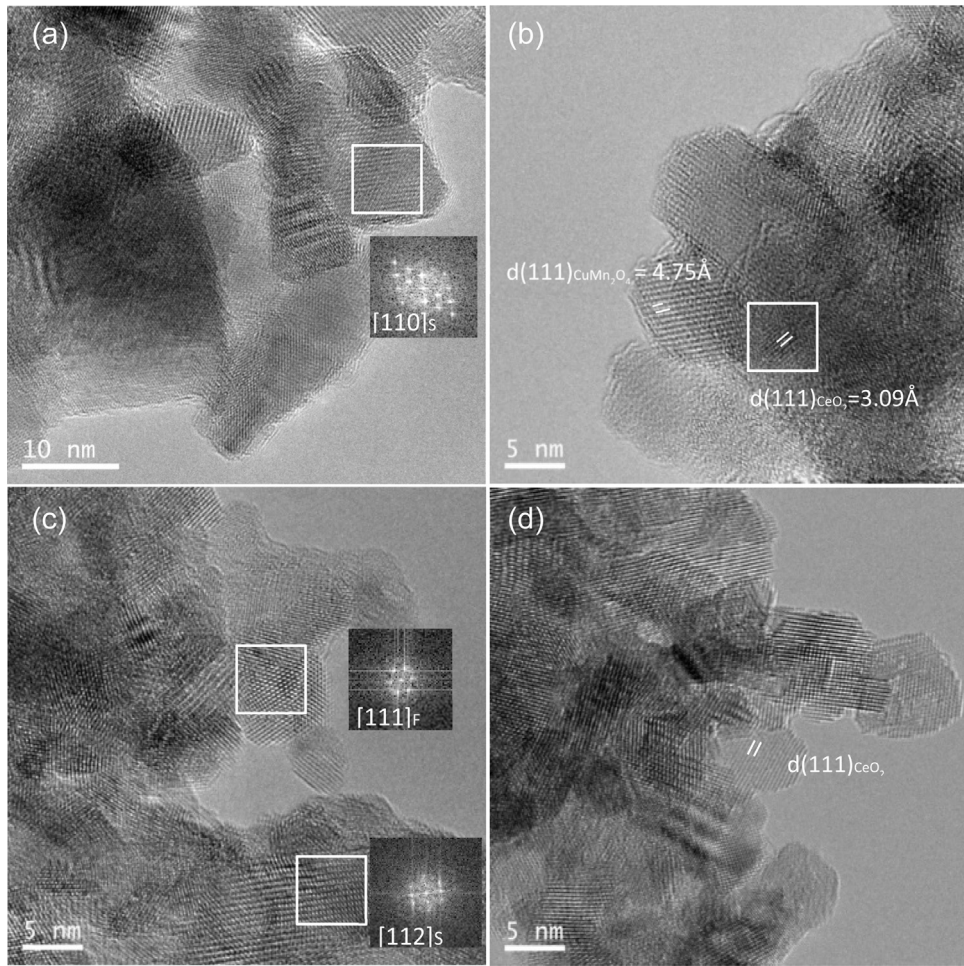


Fig. 2. HRTEM images of CuMn₂O₄ (a), and CeO₂/CuMn₂O₄ samples with 5%, 20% and 80% wt. CeO₂ in panels (b), (c), and (d), respectively. Digital diffraction patterns showing the [111] zone axis of the CeO₂ phase (fluorite) and [112] zone axis of the CuMn₂O₄ phase (spinel) are shown.

Concerning the spatial distribution of the CeO₂-nanoparticles over the CuMn₂O₄ support, as examined by XEDS analysis, elemental maps obtained in the STEM mode are presented in Fig. 3. For every composition, the three-element distribution maps (Cu, Mn and Ce) indicate on the whole that the CeO₂ phase is homogeneously distributed over the CuMn₂O₄ support. For the sample with lowest CeO₂ content (5 wt.%, Fig. 3a), the particles do not apparently cover the entire area of the support, whereas for the sample with highest CeO₂ content (80 wt.%, Fig. 3c), agglomerates of CeO₂ particles are observed which appear to some extent segregated from the CuMn₂O₄ support. In turn, the sample with intermediate CeO₂ loading (20 wt.%, Fig. 3b) exhibits a more balanced coverage of the support with ceria.

H₂-TPR experiments were performed in order to explore the redox properties of selected CeO₂/CuMn₂O₄ catalysts and the CuMn₂O₄ support, Fig. 4. The profiles observed are similar to those observed for Cu-Mn mixed oxides in which basically two reduction peaks appear, a first weak one at low temperature and a second multicomponent one, intense and broad, at higher temperature [52–54]. According to the literature the two-step reduction involve the reduction of the two cationic components of the spinel to Cu⁰ and to Mn²⁺ species although it has not been possible to attribute the individual peaks to specific redox species [52–54]. Thus, it has been proposed that the low temperature peak could correspond to the reduction of the copper and the high temperature one to the reduction of the manganese on the basis of comparison with the reduction temperature required for the reduction of CuO and

Mn₂O₃ reference samples [52,54]. Alternatively, the low temperature peak has been attributed to the reduction of Mn⁴⁺ species which may be present in the mixed oxide as a consequence of the redox equilibrium between Cu²⁺/Mn³⁺ and Cu⁺/Mn⁴⁺ [53]. In our case, the profiles of 5Ce/CuMn and 20Ce/CuMn show important similarities with the profile observed for the bare CuMn₂O₄ support. The main differences are related to a small shift of the low temperature peak in the presence of cerium from 153 °C (CuMn₂O₄) to 143 °C (5Ce/CuMn) or 146 °C (20Ce/CuMn) along with a certain enhancement of the reducibility around 200 °C and an increase in the overall amount of hydrogen consumed in the presence of cerium (integrated areas increased to 1.14 and 1.45 times that of CuMn₂O₄; note the results are normalized with respect to the amount in weight of CuMn₂O₄ present in every case); this latter can certainly be related to the partial concomitant reduction of cerium, as observed in samples which combine copper and cerium oxides [55]. Nevertheless, important changes are observed for 80Ce/CuMn in which the low temperature peak is significantly shifted down to 95 °C while the high temperature one is also apparently shifted to lower temperature; in turn, still a higher increase of the overall hydrogen consumption is observed for this sample (integrated area is 2.68 times that of CuMn₂O₄) thus revealing an increase in the amount of cerium which becomes reduced over this sample.

The surface of the CuMn₂O₄ support and selected CeO₂/CuMn₂O₄ catalysts was examined by XPS. The spectra of Ce 3d, Cu 2p_{3/2}, Mn 2p and O 1s binding energy regions of the samples are shown in Fig. 5. The spectra in the Ce 3d region

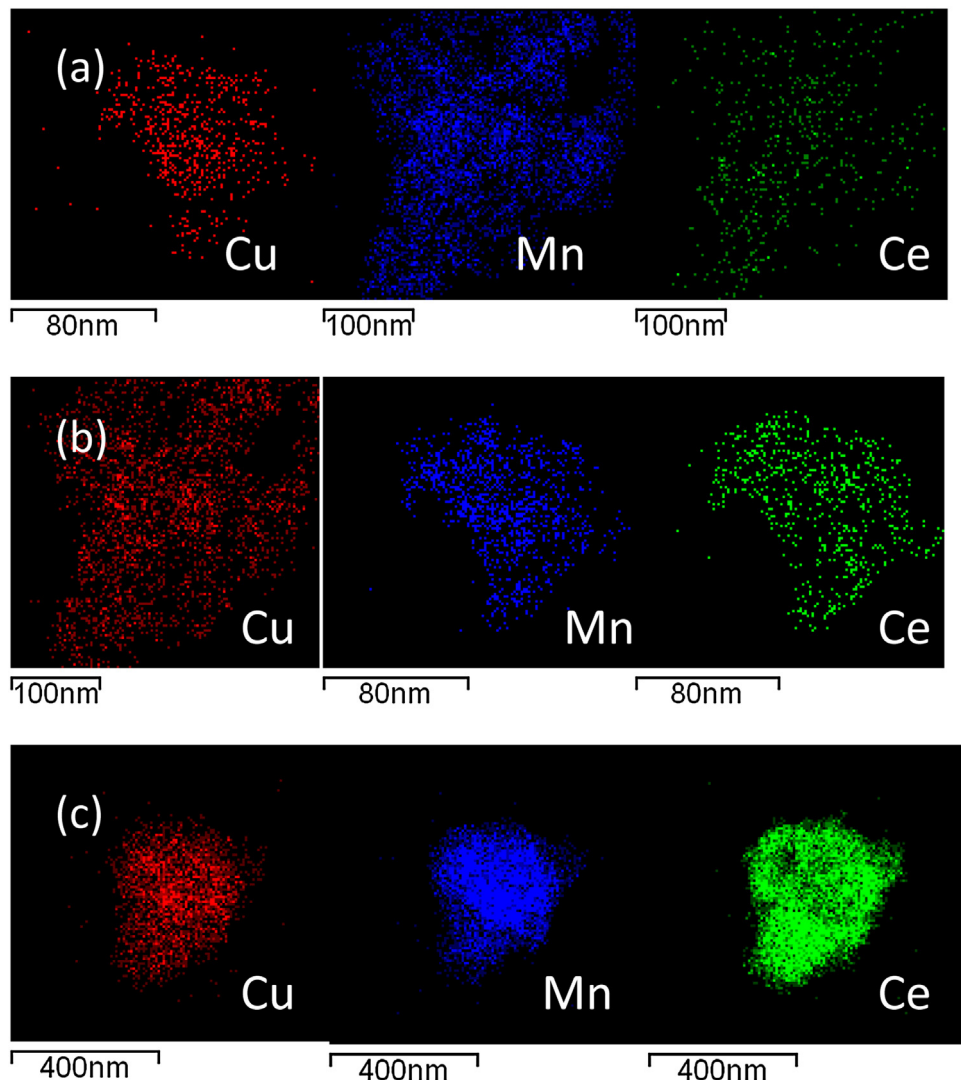


Fig. 3. XEDS elemental distribution maps of Mn, Ce and Cu for 5-Ce/CuMn (a), 20-Ce/CuMn (b) and 80-Ce/CuMn (c).

basically exhibit a set of two doublets which correspond to a deconvolution into eight peaks labelled as u ($u-u''$) for $3d_{3/2}$ and v ($v-v''$) for $3d_{5/2}$. Among them, the doublet v'/u' is considered as the fingerprint of the presence of Ce^{3+} (note this is a simplification since they correspond only to the center in each case of most intense peak or set of peaks observed for Ce_2O_3 [56]) whereas the other peaks are attributed to Ce^{4+} [28,45,56]. According to the relative contribution of Ce^{3+} features to the spectrum, 19.4, 21.9 and 20.0% of the cerium appears as Ce^{3+} in 5Ce/CuMn, 20Ce/CuMn and 80Ce/CuMn samples, respectively. The presence of reduced cerium is typical for nanostructured ceria samples and values around 20% of Ce^{3+} are found for them [28,57]. Nevertheless, it would be expected that the Ce^{3+} amount increases with decreasing the crystal size [58], which is not apparently accomplished in this case (Table 1); this suggests that the introduction of manganese (or copper) cations in the ceria fluorite lattice may help to decrease such effect for the very low size ceria nanocrystals present in samples 5Ce/CuMn and 20Ce/CuMn. Concerning the O 1s zone, two peaks are basically observed for all samples at 532.8–531.5 and 530.5–529.9 eV while sample 80Ce/CuMn exhibits a third peak at ca. 528.6 eV. The peak at 532.8–531.5 eV is typical for oxygens from chemisorbed or surface species like hydroxyls or carbonates difficult to eliminate during steps of precursor decomposition involved in the preparation and/or as a consequence of interaction

with atmospheric air [57]. The peaks at 530.5–529.9 and 528.6 eV must correspond to bulk oxygens [57]. The fact that a new peak appears at 528.6 eV for 80Ce/CuMn suggests this may correspond to oxygens in relatively big ceria crystals (Table 1).

Concerning the Cu 2p3/2 zone, all spectra are basically constituted by two main peaks at ca. 931.1 and 934.1–933.9 eV. Main difference between the samples is apparently related to a decrease in the relative contribution of the former peak with increasing the cerium content (the ratio between them is of 1.7, 2.2, 2.6 and 5.3 for CuMn_2O_4 , 5Ce/CuMn, 20Ce/CuMn and 80Ce/CuMn, respectively); in addition, an apparent broadening of the peaks is produced for 80Ce/CuMn. The peak at 934.1–933.9 eV along with satellite peaks appearing in the 947–938 eV zone can be assigned to Cu^{2+} species [57]; on the other hand, the peak located at 931.1 eV can be assigned to Cu^+ species in the tetrahedral position of the spinel [39,59]. In turn, the Mn 2p spectra reveal the presence of two $2p_{3/2}$ contributions at 642.7–641.9 and 645.0–644.1 eV which can be assigned to Mn^{3+} and Mn^{4+} species, respectively [21]. As mentioned above, the presence of Mn^{4+} and Cu^+ species is typical for CuMn_2O_4 and has been proposed to be a consequence of the redox equilibrium with $\text{Mn}^{3+}/\text{Cu}^{2+}$; the extent of electron transfer between copper and manganese normally depends on the temperature employed for the preparation of the spinel [59]. It is noted in this sense that the decrease of the Cu^+ contribution observed with increasing the

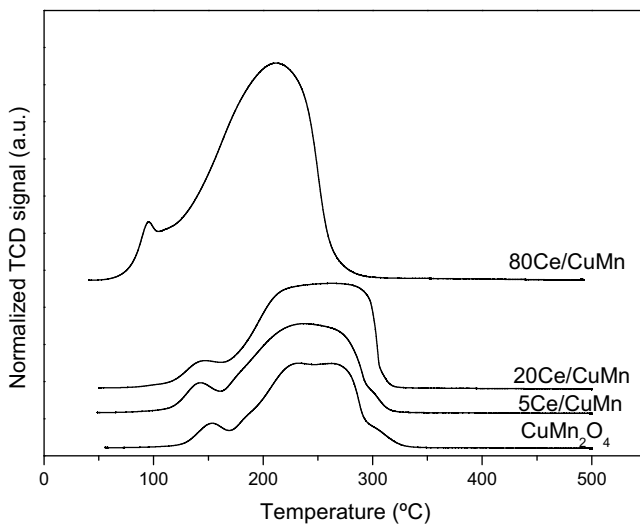


Fig. 4. H_2 consumption observed during TPR runs over the indicated catalysts. Note the consumption has been normalized with respect to the amount in weight of CuMn_2O_4 in each case.

cerium loading is not compensated by simultaneous decrease of the Mn^{4+} contribution. As in the case of the $\text{Cu} 2\text{p}$ spectra, some broadening of the $\text{Mn} 2\text{p}$ peaks is observed for 80Ce/CuMn. The observed broadening must be in any case related to the fact that most of the detected copper or manganese in 80Ce/CuMn is located at interface positions affected by interaction with the ceria component. Such interface broadening is related to the presence of local inhomogeneities at such positions with respect to bulk structure [60]. Note the same type of broadening occurs for $\text{Ce} 3\text{d}$ peaks in 5Ce/CuMn in which a higher portion of the cerium is expected to locate at interface positions than for samples with higher cerium loading.

Finally, Table 1 collects relevant atomic ratio values determined from the intensity of the XPS peaks and corrected with adequate sensitivity factors [61]. Further than expected general variations in the ratios of corresponding elements with changing the composition of the catalysts, it appears interesting that the $[\text{Cu}]/[\text{Mn}]$ ratio apparently increases with increasing the cerium loading in the samples. In turn, the relatively low concentration detected for copper or manganese in the 80Ce/CuMn sample poses doubts about the accessibility of sites at the CuMn_2O_4 support surface in this sample, as will be addressed below.

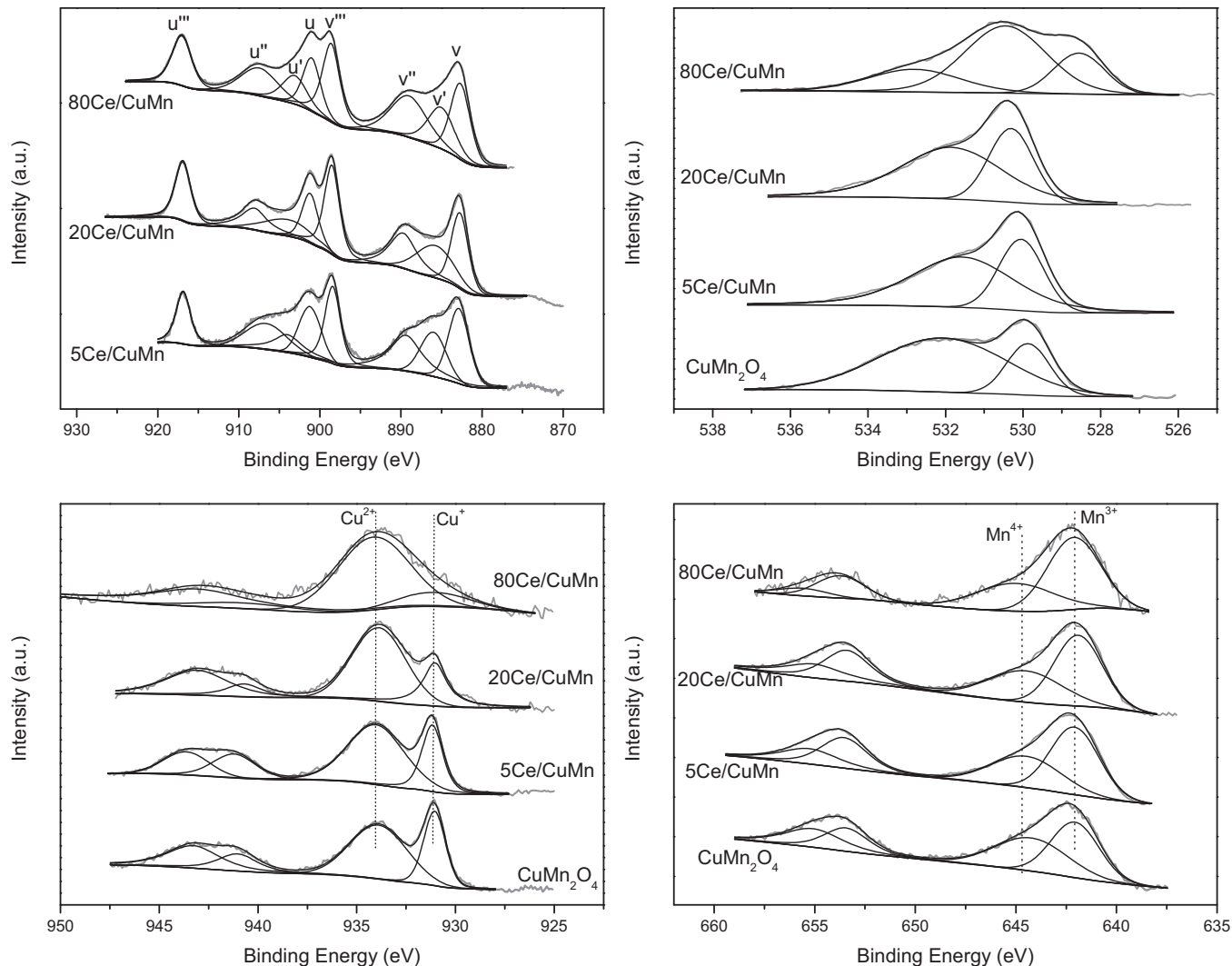


Fig. 5. XPS spectra for the indicated samples in regions Ce 3d (top left), O 1s (top right), $\text{Cu} 2\text{p}_{3/2}$ (bottom left) and $\text{Mn} 2\text{p}$ (bottom right).

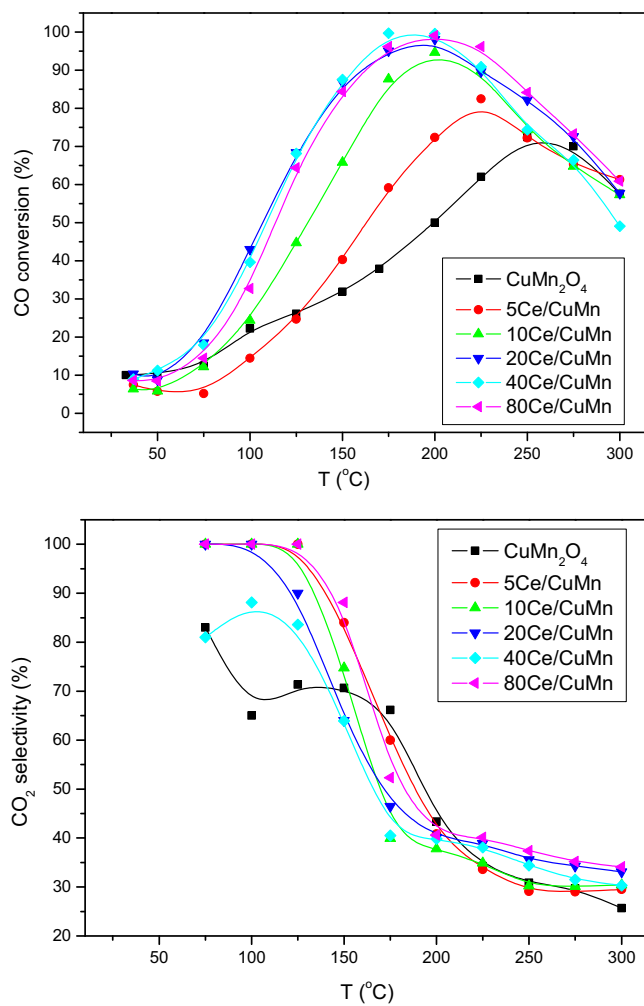


Fig. 6. CO conversion and oxygen selectivity to CO₂ during CO-PROX catalytic activity tests (1% CO + 1.25% O₂ + 50% H₂ with 0.2% H₂O, He balance) over indicated catalysts.

3.2. Catalytic properties

Activity data for the series of catalysts under CO-PROX conditions are shown in Fig. 6. The CO conversion generally increases with increasing the cerium content of the catalysts and shows a maximum around 20–40 wt.% Ce, decreasing slightly for 80Ce/CuMn. In turn, the selectivity to CO₂ apparently decreases in general terms upon increasing the cerium loading up to 40 wt.% while 80Ce/CuMn constitutes an exception in such trend and displays selectivity levels close or even higher than those of 5Ce/CuMn. This latter is also reflected in the highest CO conversion level achieved for this sample at temperatures above maximum CO conversion at which the H₂ oxidation reaction strongly compete with the CO oxidation one.

In order to get more details about the catalytic properties of these samples, a selection of them has been examined by DRIFTS under reaction conditions. Main changes observed upon interaction of the samples with the reactant mixture are observed in the zone corresponding to the C–O stretching of carbonyl species, as shown in Fig. 7. Other changes (not shown) are observed in zones corresponding to the O–H stretching mode of hydroxyl species (or water) or the C–O stretching modes of carbonate-type species; these are more apparent as the cerium content of the catalyst increases and are of minor catalytic relevancy in any case since they typically reflect exclusively the evolution of oxidation products CO₂

or H₂O [25,26,55]. In turn, Fig. 8 displays the evolution of CO₂ and H₂O during the *operando*-DRIFTS experiments and which reflect the activity for CO and H₂ oxidation, respectively. Note despite the same reactant mixture is employed as for the catalytic activity tests done with a tubular reactor (Fig. 6), some differences in conversion levels appear between both types of tests as a consequence of differences in the type of reactors employed although qualitative agreement between respective results is achieved in any case.

CuMn₂O₄ shows the formation of a carbonyl at 2125 cm⁻¹ upon interaction of the sample with the reactant mixture at 25 °C (Fig. 7a). This species can be attributed to a Cu⁺-carbonyl on the basis of comparison with carbonyls formed upon adsorption of CO on Cu₂O [62]. It grows with increasing the temperature under the reaction mixture up to 100 °C while it gradually shifts to the red down to 2118 cm⁻¹. The intensity maximum practically coincides with onset of CO oxidation (Fig. 8). Then, for higher reaction temperature, a decrease of the Cu⁺-carbonyl intensity along with a more important red shift down to 2107 cm⁻¹ is observed (Fig. 7a). In contrast, carbonyls observed for the Ce-containing samples appear at apparently lower frequency, generally increasing with the cerium loading, between 2110 and 2115 cm⁻¹ (Fig. 7). These carbonyls appear at frequencies expected for metallic copper carbonyls; however, as detailed elsewhere [63], their relatively high thermal stability indicates that they correspond to Cu⁺-carbonyls with relatively low frequency values as a consequence of their interaction with ceria. As shown in Fig. 8, the Cu⁺-carbonyls display the highest intensity at low reaction temperatures for 20Ce/CuMn. In turn, noteworthy they still display some intensity for 80Ce/CuMn despite mentioned doubts with respect to the accessibility of support sites in this sample, according to discussion of XPS results above. Nevertheless, a particularity is noted in this sample when examining the evolution of the Cu⁺-carbonyl intensity with respect to the evolution of CO₂ and H₂O products (revealing CO and H₂ oxidation reactions taking place during the CO-PROX process, respectively). Thus, the temperature at which the Cu⁺-carbonyls become extinguished practically coincides with onset of H₂ oxidation in CuMn₂O₄, 5Ce/CuMn and 20Ce/CuMn; however, they become extinguished apparently before onset of such reaction in 80Ce/CuMn (Fig. 8).

3.3. Structure/redox/activity relationships

Characterization results obtained by XRD, HRTEM and XEDS, and XPS provide a complete picture of the structural and chemical properties of the catalysts (Figs. 1–5). Thus, the catalysts are shown to be basically constituted by a nanostructured CuMn₂O₄ spinel support onto which agglomerates of primary ceria particles, more or less doped with copper or manganese heterocations, appear supported. The main difference between the samples in this sense appears related to the size of the supported ceria nanocrystals, which increases with increasing the cerium loading of the catalysts (Table 1). It must be noted that, in principle, one theoretical CeO₂ monolayer over the employed CuMn₂O₄ support (taking into account its specific surface area, Table 1) would be achieved for a ceria loading of around 10 wt.%. The observed evolution of S_{BET} as a function of ceria loading appears in line with this estimation (Table 1). The ceria particles apparently block partially the pores of the CuMn₂O₄ support leading to a small decrease of S_{BET} for Ce wt.% \leq 10. In contrast, the ceria agglomerates form a new porous structure for higher loading and lead to an important increase in the S_{BET} values for higher Ce loading. Doubts arise in any case as to the accessibility of surface sites of the support for samples with high Ce loading well above theoretical monolayer loading. This is however evidenced by the *operando*-DRIFTS results which exhibit the formation of Cu⁺-carbonyls, formed upon interaction of CO with the support surface, even for the 80Ce/CuMn sample which impor-

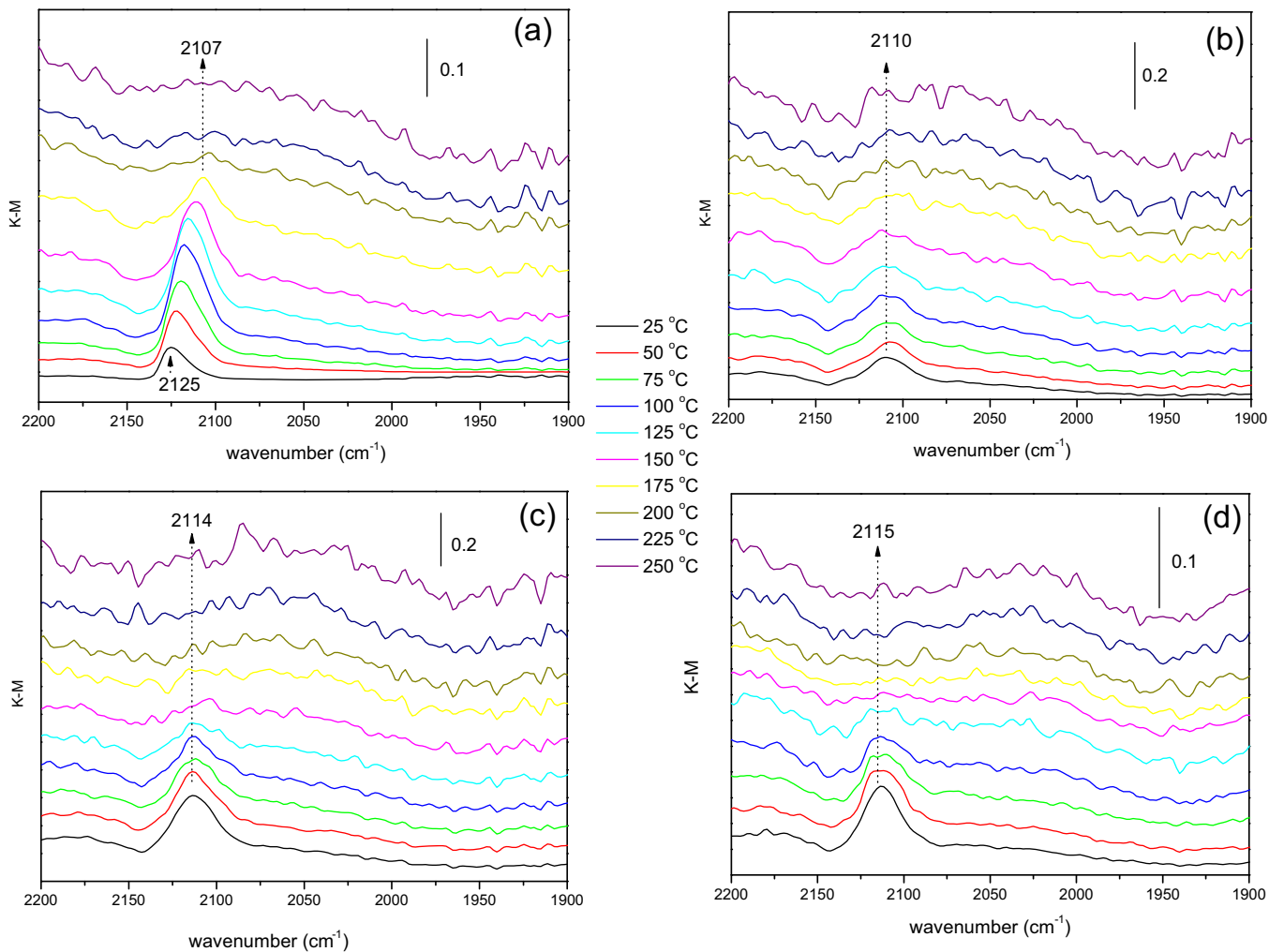


Fig. 7. DRIFTS spectra recorded under CO-PROX mixture (1% CO + 1.25% O₂ + 50% H₂ with 0.2% H₂O, He balance) at the indicated temperatures over (a) CuMn₂O₄; (b) 5Ce/CuMn; (c) 20Ce/CuMn; and (d) 80Ce/CuMn.

tantly exceeds mentioned theoretical monolayer Ce loading (Fig. 7). Nevertheless, XPS reveals that an appreciable amount of the surface exposed sites of the support in this sample must be located at interfacial positions; this is evidenced by the important broadening observed for corresponding photoelectronic signals (Fig. 4). On the basis of all characterization results, basically two different situations appear for the CeO₂/CuMn₂O₄ samples, as summarized in the scheme presented in Fig. 9. For relatively low Ce loading, small agglomerates of (more or less doped) ceria nanoparticles of very small size (Table 1) appear dispersed over the CuMn₂O₄ support and interfacial sites of the support constitute a relatively minor portion of the surface exposed centers of this component. In contrast, for high Ce loading, in particular for sample 80Ce/CuMn, the agglomerates of (more or less doped) ceria nanoparticles of bigger size form a new porous structure and cover an important portion of the support sites in such a way that an appreciable amount of those which remain exposed appear in interfacial positions, thus in principle affected by interaction with the supported ceria particles.

Such differences apparently have important consequences concerning the redox properties of the catalysts. TPR experiments reveal an important enhancement of the CuMn₂O₄ support reducibility for 80 Ce/CuMn (Fig. 4). This must be a consequence of the interfacial character of an important part of the support surface sites in this sample, as discussed above (Fig. 9). Such interfacial sites must be most reducible ones considering that ceria can

act as a promoter for their reduction, as it occurs also in catalysts combining copper and cerium oxides [55,64]. Promoting effects of ceria on the reducibility of the support also appear in 20Ce/CuMn or 5Ce/CuMn although they appear much less intense than those observed for 80Ce/CuMn (Fig. 4). Another effect of the interaction of ceria with the CuMn₂O₄ support is the relative decrease of the contribution of the Cu⁺ component to the Cu 2p_{3/2} XPS spectrum (signal at 931.1 eV) upon increasing the cerium loading of the samples. As discussed above, these Cu⁺ cations have been proposed to appear in the CuMn₂O₄ spinel phase as a consequence of redox equilibrium between Cu²⁺/Cu⁺ and Mn³⁺/Mn⁴⁺ in an amount which depends on the temperature of the thermal treatment employed for its preparation [59]. However, the gradual decrease observed in the Cu⁺ contribution upon increasing the cerium loading is not accompanied by concomitant decrease of the Mn⁴⁺ component (Fig. 5). The XPS results obtained suggest that the Cu⁺ decrease could be related to the interaction of the support with ceria which could favor the transfer of electrons from the Cu⁺ sites to the ceria nanoparticles. Yet another explanation for the observed phenomenon could be as follows. Since XRD generally reveals that the ceria nanoparticles appear as partially doped with copper or manganese heterocations, it appears that the surface cations of the support may become (even if only partially) leached during preparation of the supported catalysts upon interaction with the weakly acid (and most likely out of the PZC point of CuMn₂O₄) impregnating solution of cerium.

Thus, a part of the copper or manganese cations incorporated to the solution could coprecipitate with cerium during solvent evaporation. It may occur that manganese coprecipitates preferentially with cerium thus becoming finally incorporated to the ceria bulk. Then, copper remaining in the solution can become reincorporated to the support surface most likely in the form of small dispersed CuO patches, thus increasing the final relative amount of surface Cu²⁺ species. This could also explain the important decrease observed in the Mn/Cu atomic ratio upon increasing the cerium content of the catalysts and as inferred from the XPS data collected in Table 1. Unfortunately, it is not easy to distinguish Cu²⁺ species in CuO from those present in CuMn₂O₄ on the basis of Cu 2p XPS since practically no difference in the binding energy is expected [65]. Some more difference can be expected in this sense in the energy of the Cu_{LMM} Auger electron at its maximum which appears (as expected in any case for Cu²⁺ species, major one in any case) at E_k of 917.6 eV for CuO and at 918.0 eV for CuMn₂O₄ [65]. However, in our case, such maximum (not shown) appears at 917.8 eV for CuMn₂O₄ and at 917.7 eV for 5Ce/CuMn and 20Ce/CuMn (the relatively weak signal obtained for 80Ce/CuMn does not allow its reliable measurement for this sample). Thus, unfortunately such data do not allow achieving a more definitive conclusion in this sense. In any case, the *operando*-DRIFTS experiments (Fig. 7) also provide support to the change in the type of exposed copper sites at the surface. Contact of the CO-PROX mixture with CuMn₂O₄ sample at 25 °C produces a Cu⁺-carbonyl at 2125 cm⁻¹ which may well form upon adsorption of CO on the surface exposed Cu⁺ sites at the spinel tetrahedral positions. Such carbonyl at 2125 cm⁻¹ is however missing for Ce-containing samples which basically display, as discussed above, interfacial Cu⁺-carbonyls, typically formed by interfacial reduction under the CO-PROX mixture [26,66].

The CO oxidation activity under the CO-PROX mixture exhibits a general increase with increasing the amount of cerium in the catalysts, at least up to 40 wt.%. This must be attributed to the presence of increasing amounts of CeO₂—CuMn₂O₄ interfacial sites upon increasing the cerium loading; such interfacial sites have been proposed to be most active ones for CO oxidation in catalysts combining copper and cerium oxides [25,26]. This is reflected by the increase of the amount of Cu⁺ carbonyls under reaction conditions which displays a maximum (among the catalysts explored by DRIFTS) for 20Ce/CuMn (Fig. 8); note in this sense that the CO oxidation rate under CO-PROX conditions has been shown to be proportional to the intensity of the interfacial Cu⁺-carbonyls in catalysts combining copper and cerium oxides [26]. As mentioned above, such Cu⁺-carbonyls have been proposed to be formed after partial reduction of the initially oxidized interfacial sites upon interaction with the CO-PROX mixture [25,26,66]. In this respect, a different situation is apparently found for CuMn₂O₄. As discussed above, interaction of the CO-PROX mixture with the sample at 25 °C produces the Cu⁺-carbonyl at 2125 cm⁻¹ upon adsorption of CO in the reactant mixture over the exposed Cu⁺ cations originally present. Then, the increase in the intensity of Cu⁺-carbonyls up to 100 °C (Figs. 7a and 8) must reflect the reduction of the surface Cu²⁺ at the tetrahedral sites of the spinel. Such reduction process produces a red shift of the Cu⁺-carbonyl which is related to an increase in the π -back-bond component in them, within the usual σ bond- π -back-bond scheme employed to explain carbonyl bonds in this type of species [62,63,67], favored by the increase of the electron density upon increasing the reduction level of the oxide. Thus, onset of CO oxidation activity in this sample only takes place when a certain reduction level is attained which suggests such reduced state as the active one for the reaction. Nevertheless, the fact that the Cu⁺-carbonyls display higher intensity at that onset point in CuMn₂O₄ than found for the Ce-containing samples strongly suggests the lower intrinsic activity of the active sites in CuMn₂O₄ in comparison with those at the CeO₂—CuMn₂O₄ interface.

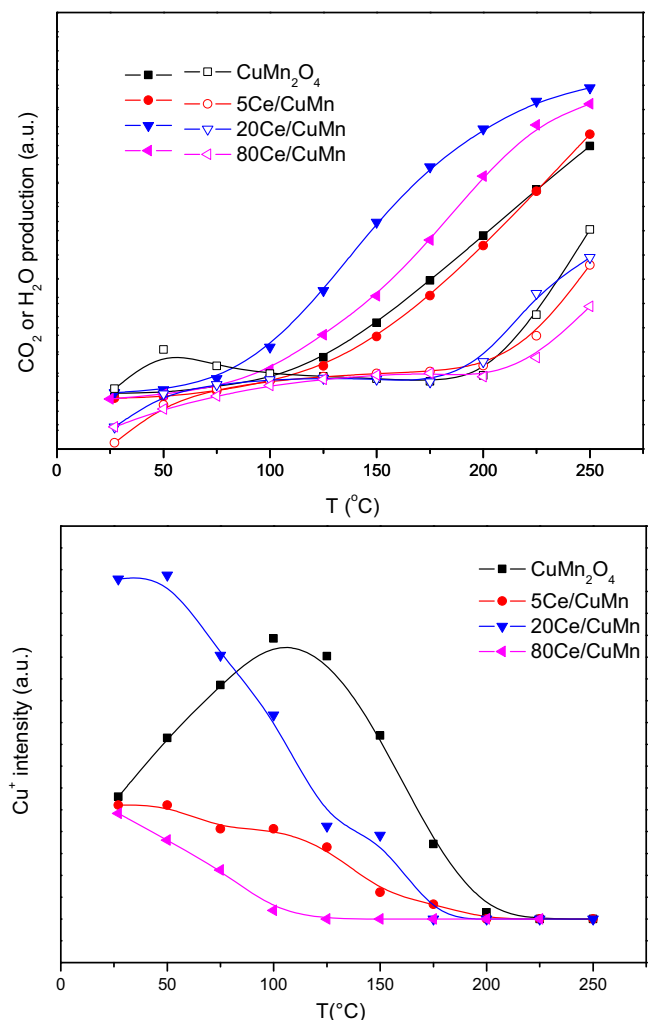


Fig. 8. MS evolution of signals corresponding to $m/e = 44$ (CO₂, full symbols) and $m/e = 18$ (H₂O, open symbols) (top) and of the Cu⁺ carbonyl intensity (bottom) during the DRIFTS experiments under CO-PROX mixture.

In turn, for CeO₂/CuMn₂O₄ catalysts, the selectivity of O₂ towards formation of CO₂ (or, as simplified, the CO₂ selectivity) apparently decreases with increasing the cerium loading up to 40 wt.%. This result must be basically attributed to the changes observed in the size of the CeO₂ crystals (Table 1). As noted before in CeO₂/CuO catalysts, the CO₂ selectivity increases with decreasing the size of the supported ceria crystals [68]. This has been attributed to a favored hindering of the reduction of interfacial copper sites upon decreasing the size of the interacting ceria crystals which is in turn most likely related to a more favored transfer of electrons from copper to ceria in such case [68]. This is supported by the *operando*-DRIFTS results (Figs. 7 and 8). As noted before, careful analysis of Fig. 8 shows that onset of H₂ oxidation (revealed by the observed increase in H₂O) is produced at the point when the Cu⁺-carbonyls become extinguished. Taking into account that the p_{CO} at that point is still appreciable (since CO conversion is still well below its maximum and therefore unreacted CO must remain available) it would be expected that Cu⁺-carbonyls would be formed if Cu⁺ species remain exposed at the surface and given the relatively high thermal stability of such type of carbonyls [63]. Thus, the extinction of the carbonyls in those conditions suggests that copper becomes reduced to the metallic state onto which corresponding carbonyls would be thermally unstable and have relatively low lifetime which would prevent their detection. Achievement of such strong reduction level in the copper would favor H₂ oxidation since the metallic

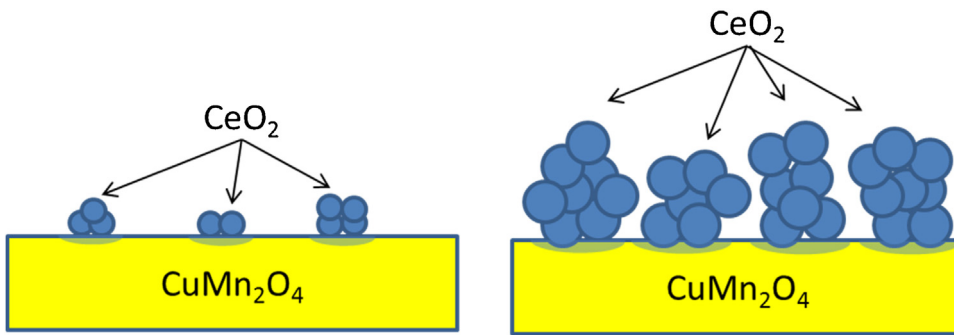


Fig. 9. Scheme of the two characteristic situations found for the $\text{CeO}_2/\text{CuMn}_2\text{O}_4$ catalysts. Basically, there appear differences in the size of the (more or less doped with manganese or copper heterocations) as well as in the interfacial character of surface exposed sites of the support. These are illustrated as shadowed regions in the pictures.

state of copper can be most likely the most active for such reaction [26,68].

The 80Ce/CuMn sample apparently constitutes a particular case among the series of catalysts in this sense. Its particular structural characteristics in which the relatively high amount of cerium in it finally determines an interfacial character for an important portion of the surface exposed sites of the support (Fig. 9) must certainly be invoked to explain its particular properties. First, somewhat smaller CO oxidation activity is observed over it than for samples with lower Ce loading like 40Ce/CuMn or 20Ce/CuMn (Figs. 6 and 8). According to the *operando*-DRIFTS results in which lower Cu^+ -carbonyl intensity is detected for 80Ce/CuMn, this must be related to the fact that a relatively lower amount of CeO_2 – CuMn_2O_4 interfacial sites are formed in this sample as a consequence of the high cerium loading. In second place, it displays a relatively high CO_2 selectivity despite the fact that CeO_2 crystals show the largest size among the series of samples (Table 1). It is also noted that the Cu^+ -carbonyls become extinguished at relatively low temperature in this sample, much before onset of H_2 oxidation (Fig. 8), which contrasts with observation for the other samples as discussed above. A possible hypothesis to explain such results is the following. Since most of the active copper sites in this sample are located at interfacial positions and therefore affected by interaction with ceria, the electron transfer from copper to ceria can help to maintain the exposed copper entities in a Cu^+ state, thus retarding the formation of metallic copper active for H_2 oxidation under the CO-PROX mixture; the metallic copper sites could most likely be stabilized at positions far from the interface at which their interaction with the supported ceria nanoparticles would be weaker [26]. Thus, synergistic effects between the two components would be maximized in this sample. These would involve the electron transfer from metallic copper to ceria which would preserve active interfacial Cu^+ species onto which CO becomes activated; such electron transfer will simultaneously favor the activation of O_2 for its reduction on the surface of the ceria component by increasing the reduction degree of this component. The premature decrease in the Cu^+ -carbonyl intensity observed for this sample (Fig. 8) can be related to the fact that the sites onto which the carbonyls are formed at relatively low temperature operate themselves as active sites when the reaction rate increases upon increasing the reaction temperature. The relatively low lifetime of Cu^+ -carbonyls eventually participating as intermediates (in contrast to those which are detected and which would correspond to spectator species) in such case would prevent their detection under employed conditions.

4. Conclusions

A CuMn_2O_4 support has been prepared by a microemulsion method and shown to be constituted by aggregates of spinel nanocrystals with ca. 16 nm average size. Catalysts of ceria sup-

ported on CuMn_2O_4 prepared by impregnation appear constituted by agglomerates of nanocrystals of ceria doped with heterocations from the support (most likely manganese) homogeneously dispersed on the CuMn_2O_4 support, on the basis of XRD, HRTEM and XEDS results. Differences which appear as a function of the cerium loading (between 5 and 80 wt.%) are related first to the textural properties of the samples. The theoretical monolayer loading (around 10 wt.%) apparently marks a turning point which determines the S_{BET} values observed: below such point, the supported ceria particles apparently block the pores of the support leading to some decrease of S_{BET} ; above such point the aggregates of ceria nanocrystals apparently form a new porous structure leading to increase of the S_{BET} values for the samples. A second important difference as a function of the cerium loading is related to the size of the supported (doped with copper or manganese heterocations) ceria nanocrystals with important implications for the CO-PROX properties of the catalysts. An increase of the selectivity of O_2 towards formation of CO_2 (CO_2 selectivity) is generally observed upon decreasing the (doped) ceria crystal size. This has been related to an enhanced synergistic effect between the two catalyst components which helps to prevent formation of the metallic state of copper under reaction conditions, on the basis of *operando*-DRIFTS experiments. In any case, the CO oxidation activity achieved basically depends on the amount of active interfacial sites created between the two components in every case and whose amount generally increases with the cerium loading up to 40 wt.%. The sample with 80 wt.% of Ce constitutes a special case. Because of its high cerium loading, the aggregates of ceria importantly cover the support and limit the amount of support sites exposed at its surface, as evidenced during the *operando*-DRIFTS experiments. This imposes an interfacial character to an important portion of the surface exposed sites of the support, as evidenced by XPS. The main catalytic consequence of such particular configuration is the enhanced CO_2 selectivity exhibited by this sample despite the relatively large size of the supported (doped) ceria nanocrystals in it. Another interesting effect of the increase of the Ce loading is the gradual decrease observed in the relative amount of Cu^+ present at the CuMn_2O_4 support surface, according to XPS. This can be related to the redox interaction with the supported (doped) ceria nanoparticles although we cannot fully discard that it results as a consequence of partial dissolution of the support surface during impregnation and reprecipitation of the copper in the form of CuO patches during preparation steps.

Acknowledgements

Thanks are due to ICP-CSIC Unidad de Apoyo for the measurement of a part of the characterization results presented. This work

was funded by the Ministerio de Economía, Industria y Competitividad (Plan Nacional Project CTQ2015-71823-R).

References

- [1] J.R. Rostrup-Nielsen, J. Sehested, J.K. Norskov, *Adv. Catal.* 47 (2002) 65–138.
- [2] R.A. Lemons, *J. Power Sourc.* 29 (1990) 251–264.
- [3] Q. Li, R. He, J.A. Gao, J.O. Jensen, N. Bjerrum, *Electrochim Soc J.* 150 (2003) A1599–A1605.
- [4] C. Ratnasamy, J.P. Wagner, *Catal. Rev. Sci. Eng.* 51 (2009) 325–440.
- [5] J.M. Zalc, D.G. Loffler, *J. Power Sourc.* 111 (2002) 58–64.
- [6] E.S. Park, D. Lee, H.C. Lee, *Catal. Today* 139 (2009) 280–290.
- [7] N. Bion, F. Epron, M. Moreno, F. Mariño, D. Duprez, *Top. Catal.* 51 (2008) 76–88.
- [8] S.H. Oh, R.M. Sinkevitch, *J. Catal.* 142 (1993) 254–262.
- [9] M.M. Schubert, M.J. Kahlich, H.A. Gasteiger, R.J. Behm, *J. Power Source* 84 (1999) 175–182.
- [10] M. Watanabe, H. Igarashi, M. Suzuki, Y. Sasaki, H. Uchida, *Appl. Catal. A* 159 (1997) 159–169.
- [11] P.V. Snytnikov, V.A. Sobyanin, V.D. Belyaev, P.G. Tsyrulnikov, N.B. Shitova, D.A. Shlyapin, *Appl. Catal. A* 239 (2003) 149–156.
- [12] I.H. Son, A.M. Lane, *Catal. Lett.* 76 (2001) 151–154.
- [13] O. Korotikh, R. Farrauto, *Catal. Today* 62 (2000) 249–254.
- [14] S.H. Lee, J. Han, K.Y. Lee, *J. Power Source* 109 (2002) 394–402.
- [15] G.K. Bethke, H.H. Hung, *Appl. Catal. A* 194–195 (2000) 43–53.
- [16] M.M. Schubert, V. Plzak, J. Garche, R.J. Behm, *Catal. Lett.* 76 (2001) 143–150.
- [17] R.J.H. Grisel, B.E. Nieuwenhuys, *J. Catal.* 199 (2001) 48–59.
- [18] G. Avgouropoulos, T. Ioannides, H.K. Matralis, J. Batista, S. Hocevar, *Catal. Lett.* 73 (2001) 33–39.
- [19] F. Marino, C. Descorme, D. Duprez, *Appl. Catal. B* 58 (2005) 175–183.
- [20] A. Martínez-Arias, A.B. Hungría, M. Fernández-García, J.C. Conesa, G. Munuera, *J. Power Source* 151 (2005) 32–42.
- [21] E. Moretti, M. Lenarda, L. Storaro, A. Talon, T. Montanari, G. Busca, E. Rodríguez-Castellón, A. Jiménez-López, M. Turco, G. Bagnasco, R. Frattini, *Appl. Catal. A* 335 (2008) 46–55.
- [22] G. Avgouropoulos, T. Ioannides, Ch. Papadopoulou, J. Batista, S. Hocevar, H.K. Matralis, *Catal. Today* 75 (2002) 157–167.
- [23] W. Liu, A.F. Sarofim, M. Flytzani-Stephanopoulos, *Chem. Eng. Sci.* 49 (1995) 4871–4888.
- [24] A. Martínez-Arias, M. Fernández-García, O. Gálvez, J.M. Coronado, J.A. Anderson, J.C. Conesa, J. Soria, G. Munuera, *J. Catal.* 195 (2000) 207–215.
- [25] D. Gamarra, G. Munuera, A.B. Hungría, M. Fernández-García, J.C. Conesa, P.A. Midgley, X.Q. Wang, J.C. Hanson, J.A. Rodriguez, A. Martínez-Arias, *J. Phys. Chem. C* 111 (2007) 11026–11038.
- [26] D. Gamarra, C. Belver, M. Fernández-García, A. Martínez-Arias, *J. Am. Chem. Soc.* 129 (2007) 12064–12065.
- [27] A. Kubacka, A. Martínez-Arias, M. Fernández-García, *ChemCatChem* 7 (2015) 3614–3624.
- [28] A. Elmhamdi, R. Castañeda, A. Kubacka, L. Pascual, K. Nahdi, A. Martínez-Arias, *Appl. Catal. B* 188 (2016) 292–304.
- [29] T.H. Rogers, C.S. Piggot, W.H. Bahlke, J.M. Jennings, *J. Am. Chem. Soc.* 43 (1921) 1973–1982.
- [30] D.R. Merrill, C.C. Scalione, *J. Am. Chem. Soc.* 43 (1921) 1982–2002.
- [31] M.A. Brittan, H. Bliss, C.A. Walker, *AIChE J.* 16 (1970) 305–314.
- [32] S. Vepřek, D.L. Cocke, S. Kehl, H.R. Oswald, *J. Catal.* 100 (1986) 250–263.
- [33] C. Yoon, D.L. Cocke, *J. Catal.* 113 (1988) 267–280.
- [34] G.J. Hutchings, A.A. Mirzaei, R.W. Joyner, M.R.H. Siddiqui, S.H. Taylor, *Catal. Lett.* 42 (1996) 21–24.
- [35] G.J. Hutchings, A.A. Mirzaei, R.W. Joyner, M.R.H. Siddiqui, S.H. Taylor, *Appl. Catal. A* 166 (1998) 143–152.
- [36] M. Krämer, T. Schmidt, K. Stöwe, W.F. Maier, *Appl. Catal. A* 302 (2006) 257–263.
- [37] M. Li, D.H. Wang, X.C. Shi, Z.T. Zhang, T.X. Dong, *Sep. Purif. Technol.* 57 (2007) 147–151.
- [38] Y.I. Hasegawa, R.U. Maki, M. Sano, T. Miyake, *Appl. Catal. A* 371 (2009) 67–72.
- [39] T. Valdés-Solís, I. López, G. Marbán, *Int. J. Hydrogen Energy* 35 (2010) 1879–1887.
- [40] J. Li, P. Zhu, R. Zhou, *J. Power Source* 196 (2011) 9590–9598.
- [41] H. Jin, R. You, S. Zhou, K. Ma, M. Meng, L. Zheng, J. Zhang, T. Hu, *Int. J. Hydrogen Energy* 40 (2015) 3919–3931.
- [42] X.L. Guo, J. Li, R.X. Zhou, *Fuel* 163 (2016) 56–64.
- [43] A. Hornés, A.B. Hungría, P. Bera, A. López Cámara, M. Fernández-García, A. Martínez-Arias, L. Barrio, M. Estrella, G. Zhou, J.A. Fonseca, J. Hanson, J.A. Rodriguez, *J. Am. Chem. Soc.* 132 (2010) 34–35.
- [44] A. Martínez-Arias, M. Fernández-García, V. Ballesteros, L.N. Salamanca, J.C. Conesa, C. Otero, J. Soria, *Langmuir* 15 (1999) 4796–4802.
- [45] A. Martínez-Arias, M. Fernández-García, A.B. Hungría, J.C. Conesa, G. Munuera, *J. Phys. Chem. B* 107 (2003) 2667–2677.
- [46] D. Gamarra, A. Martínez-Arias, *J. Catal.* 263 (2009) 189–195.
- [47] A. Meenakshisundaram, N. Gunasekaran, V. Srinivasan, *Phys. St. Sol. A* 69 (1982) 15–19.
- [48] H. Lu, X. Kong, H. Huang, Y. Zhou, Y. Chen, *J. Env. Sci.* 32 (2015) 102–107.
- [49] C.H.Y. Kang, H. Kusaba, H. Yahiro, K. Sasaki, Y. Teraoka, *Sol. St. Ion.* 177 (2006) 1799–1802.
- [50] B. Murugan, A.V. Ramaswamy, D. Srinivas, C.S. Gopinath, V. Ramaswamy, *Chem. Mater.* 17 (2005) 3983–3993.
- [51] P. Zhang, H. Lu, Y. Zhou, L. Zhang, Z. Wu, S. Yang, H. Shi, Q. Zhu, Y. Chen, S. Dai, *Nat. Comm.* 6 (2015), <http://dx.doi.org/10.1038/ncomms9446>.
- [52] F.C. Buciuman, F. Patcas, T. Hahn, *Chem. Eng. Proc.* 38 (1999) 563–569.
- [53] A.S. Reddy, C.S. Gopinath, S. Chilukuri, *J. Catal.* 243 (2006) 278–291.
- [54] X. Li, J. Xu, L. Zhou, F. Wang, J. Gao, C. Chen, J. Ning, H. Ma, *Catal. Lett.* 110 (2006) 149–154.
- [55] D. Gamarra, A. López Cámara, M. Monte, S.B. Rasmussen, L.E. Chinchilla, A.B. Hungría, G. Munuera, N. Gyorffy, Z. Schay, V. Cortés Corberán, J.C. Conesa, A. Martínez-Arias, *Appl. Catal. B* 130–131 (2013) 224–238.
- [56] J.P. Holgado, R. Alvarez, G. Munuera, *Appl. Surf. Sci.* 161 (2000) 301–315.
- [57] M. Monte, G. Munuera, D. Costa, J.C. Conesa, A. Martínez-Arias, *Phys. Chem. Chem. Phys.* 17 (2015) 29995–30004.
- [58] M. Fernández-García, A. Martínez-Arias, J.C. Hanson, J.A. Rodriguez, *Chem. Rev.* 104 (2004) 4063–4104.
- [59] B. Gillot, S. Buguet, E. Kester, *J. Mater. Chem.* 7 (1997) 2513–2517.
- [60] R. Reiche, S. Oswald, F. Yubero, J.P. Espinós, J.P. Holgado, A.R. González-Elipe, J. *Phys. Chem. B* 108 (2004) 9905–9913.
- [61] C.D. Wagner, L.E. Davis, M.V. Zeller, J.A. Taylor, R.H. Raymond, L.H. Gale, *Surf. Interf. Anal.* 3 (1981) 211–225.
- [62] D. Scarano, S. Bordiga, C. Lamberti, G. Spoto, G. Ricchiardi, A. Zecchina, C. Otero Areán, *Surf. Sci.* 411 (1998) 272–285.
- [63] P. Bera, A. López Cámara, A. Hornés, A. Martínez-Arias, *J. Phys. Chem. C* 113 (2009) 10689–10695.
- [64] A. Pintar, J. Batista, S. Hocevar, *J. Coll. Interf. Sci.* 285 (2005) 218–231.
- [65] P. Porta, G. Moretti, M. Musicanti, A. Nardella, *Sol. St. Ion.* 63–65 (1993) 257–267.
- [66] A. Martínez-Arias, A.B. Hungría, M. Fernández-García, A. Iglesias-Juez, J. Soria, J.C. Conesa, J.A. Anderson, G. Munuera, *Phys. Chem. Chem. Phys.* 14 (2012) 2144–2151.
- [67] P. Hollins, *Surf. Sci. Rep.* 16 (1992) 51–94.
- [68] A. López Cámara, V. Corteíz Corberáin, L. Barrio, G. Zhou, R. Si, J.C. Hanson, M. Monte, J.C. Conesa, J.A. Rodriguez, A. Martínez-Arias, *J. Phys. Chem. C* 118 (2014) 9030–9041.